Geochemistry Geophysics Geosystems G3

Article
Volume 13, Number 1
2 November 2012
Q0AG13, doi:10.1029/2012GC004454
ISSN: 1525-2027

Published by AGU and the Geochemical Society

Three-dimensional seismic structure of a Mid-Atlantic Ridge segment characterized by active detachment faulting (Trans-Atlantic Geotraverse, 25°55′N-26°20′N)

Minghui Zhao
Key Laboratory of Marginal Sea Geology, South China Sea Institute of Oceanology, Chinese Academy of Sciences, Guangzhou 510301, China (mhzhao@scsio.ac.cn)

Juan Pablo Canales and Robert A. Sohn
Woods Hole Oceanographic Institution, Woods Hole, Massachusetts 02543, USA (jpcanales@whoi.edu; rsohn@whoi.edu)

[1] We use air gun shots recorded by ocean bottom seismometers (OBSs) to generate a three-dimensional (3D) *P*-wave tomographic velocity model of the Trans-Atlantic Geotraverse (TAG) segment of the Mid-Atlantic Ridge, and to search for evidence of reflections from a shallow crustal fault interface. Near-vertical reflections were observed in some of the seismic records from OBSs deployed within the active seismicity zone defined by microearthquake hypocenters. Forward modeling of synthetic seismograms indicates that these reflections are consistent with a fault interface dipping at a low angle toward the ridge axis. Our observations suggest that the fault zone may extend beneath the volcanic blocks forming the eastern valley wall. Our 3D tomographic results show that the across-axis structural asymmetry associated with detachment faulting extends at least 15 km to the east of the ridge axis, indicating that detachment faulting and uplifting of deep lithologies has been occurring at the TAG segment for at least the last ∼1.35 Myr. The velocity model contains a 5 km by 8 km velocity anomaly within the detachment footwall. This anomaly, which is present beneath the active TAG hydrothermal mound, is characterized by a velocity inversion at 1.5–2.0 km below seafloor underlain by reduced *P*-wave velocities (∼6.2–6.5 km/s compared to surrounding areas ∼7.0–7.2 km/s) extending down to 3.5 km below seafloor. The velocity anomaly likely results from some combination of thermal and/or hydrothermal processes, and in either case our results suggest that hydrothermal fluids circulate within the upper section of the detachment footwall beneath the active mound.

Components: 11,000 words, 10 figures.

Keywords: 3D seismic structure; Mid-Atlantic Ridge; TAG hydrothermal field; active detachment fault.

Index Terms: 7220 Seismology: Oceanic crust; 7245 Seismology: Mid-ocean ridges; 8135 Tectonophysics: Hydrothermal systems (0450, 1034, 3017, 3616, 4832, 8424).

Received 21 September 2012; **Revised** 8 October 2012; **Accepted** 8 October 2012; **Published** 2 November 2012.

Zhao, M., J. P. Canales, and R. A. Sohn (2012), Three-dimensional seismic structure of a Mid-Atlantic Ridge segment characterized by active detachment faulting (Trans-Atlantic Geotraverse, 25°55′N-26°20′N), *Geochem. Geophys. Geosyst.*, *13*, Q0AG13, doi:10.1029/2012GC004454.

Theme: Oceanic Detachment Faults

1. Introduction

[2] It has been long recognized that slip along oceanic detachments faults (ODFs) formed at mid-ocean ridges (MORs) is responsible for seafloor exposures of lower crustal and upper mantle rocks [*Dick et al.*, 1981; *Karson and Dick*, 1983]. Observations of mafic and ultramafic exposures forming oceanic core complexes (OCCs) [*Karson and Lawrence*, 1997] at or near the ends of slow-spreading segments, where magma supply from the mantle is thought to be low and intermittent [*Cannat*, 1993; *Cannat et al.*, 1995], contributed to initial conceptual models in which ODFs develop and evolve along magma-poor MORs during periods of amagmatic seafloor spreading [e.g., *Tucholke and Lin*, 1994]. However, those models have evolved during the last decade as more geological and geophysical observations became available [e.g., *Canales et al.*, 2008; *Escartín et al.*, 2003; *Ildefonse et al.*, 2007; *MacLeod et al.*, 2002; *Smith et al.*, 2008; *Tucholke et al.*, 2008], and it has been recently recognized that detachment faulting is a fundamental mode of accretion for oceanic lithosphere [*Escartín and Canales*, 2011; *Escartín et al.*, 2008; *Smith et al.*, 2006].

[3] The dome-shaped fault exposures have historically been described as low-angle normal faults [*Dick et al.*, 1981; *Mutter and Karson*, 1992; *Tucholke and Lin*, 1994] because they typically dip ∼15°–30° where they break the seafloor [*Tucholke et al.*, 1998], but recent observations and numerical models indicate that they initiate at high angles. Microearthquakes observed at the Trans-Atlantic Geotraverse (TAG) segment of the Mid-Atlantic Ridge (MAR) dip at ∼70° in the lower crust [*deMartin et al.*, 2007], and paleomagnetic reconstructions from samples drilled at two MAR OCCs (Atlantis Massif OCC and a detachment fault north of the Fifteen-Twenty fracture zone) are consistent with large (50°–80°) footwall rotations during the exhumation of mafic and ultra-mafic lithologies [*Garcés and Gee*, 2007; *Morris et al.*, 2009]. These results are consistent with so-called rolling hinge models of flexure and rotation during normal fault evolution [e.g., *Buck*, 1988; *Lavier et al.*, 1999].

[4] Several studies have provided insights into the subsurface structure of OCCs, including crustal thickness and large-scale lithological variations [e.g., *Canales et al.*, 2008; *Dannowski et al.*, 2010; *Henig et al.*, 2012; *Ohara et al.*, 2007; *Planert et al.*, 2010; *Xu et al.*, 2009]. However, the only constraints to-date on the geometry of active detachment faults come from the 2003–2004 Seismicity and Structure of the TAG Segment (STAG) experiment [*Canales et al.*, 2007; *deMartin et al.*, 2007]. Hypocenters from this study delineate a steep (∼70°) fault surface at depths from 3 to 7 km that is curved in plan view, indicating a dome-shaped structure. The asymmetric seismic velocity structure in the shallow crust (<2 km below seafloor, bsf) suggests uplift along a low-angle (∼20°) fault. These results have been interpreted as indicating that the TAG detachment is formed by a single fault system that rotates from a dip of ∼70° to ∼20° at a depth of ∼2–3 km below the seafloor.

[5] In this paper we extend the STAG results by performing a three-dimensional tomographic inversion of the active-source *P*-wave first arrivals recorded on ocean bottom seismometers (OBSs) (previous inversions were performed on 2D lines), and by documenting the presence of reflected phases in the active-source OBS records that strongly suggest the existence of a fault interface in the shallow crust. We discuss the implications of our new results for the geometry and rotation of the detachment fault, and the structure of the footwall beneath the active TAG hydrothermal mound.

2. Background

2.1. Geological Setting

[6] The TAG segment is located along the MAR between 25°55′N and 26°20′N (Figure 1), bounded by two right-stepping non-transform offsets [*Sempéré et al.*, 1990]. The rift valley floor at the segment ends is characterized by deep (4,000–4,500 m) nodal basins, and shoals toward the segment center up to ∼3,700 m. The rift valley walls show a pronounced asymmetry at the segment center, with more elevated topography along the eastern flank than along the western flank (Figure 1). The absence of a well-developed mantle Bouguer gravity anomaly in the TAG segment [*Fujimoto et al.*, 1996] (a feature commonly observed in many other MAR segments [e.g., *Detrick et al.*, 1995; *Lin et al.*, 1990]) suggests relatively high rock densities at shallow levels.

[7] Structurally, the rift valley floor is characterized by a discontinuous, ∼4-km-wide neovolcanic zone of unfissured volcanics [*Kleinrock and Humphris*, 1996] (Figure 1). The neovolcanic zone is flanked to the east by a highly fissured zone that hosts the TAG hydrothermal field [*Kleinrock and Humphris*, 1996]. The hydrothermal field is comprised of a low-temperature alteration zone and several high-temperature hydrothermal deposits [*Rona et al.*,

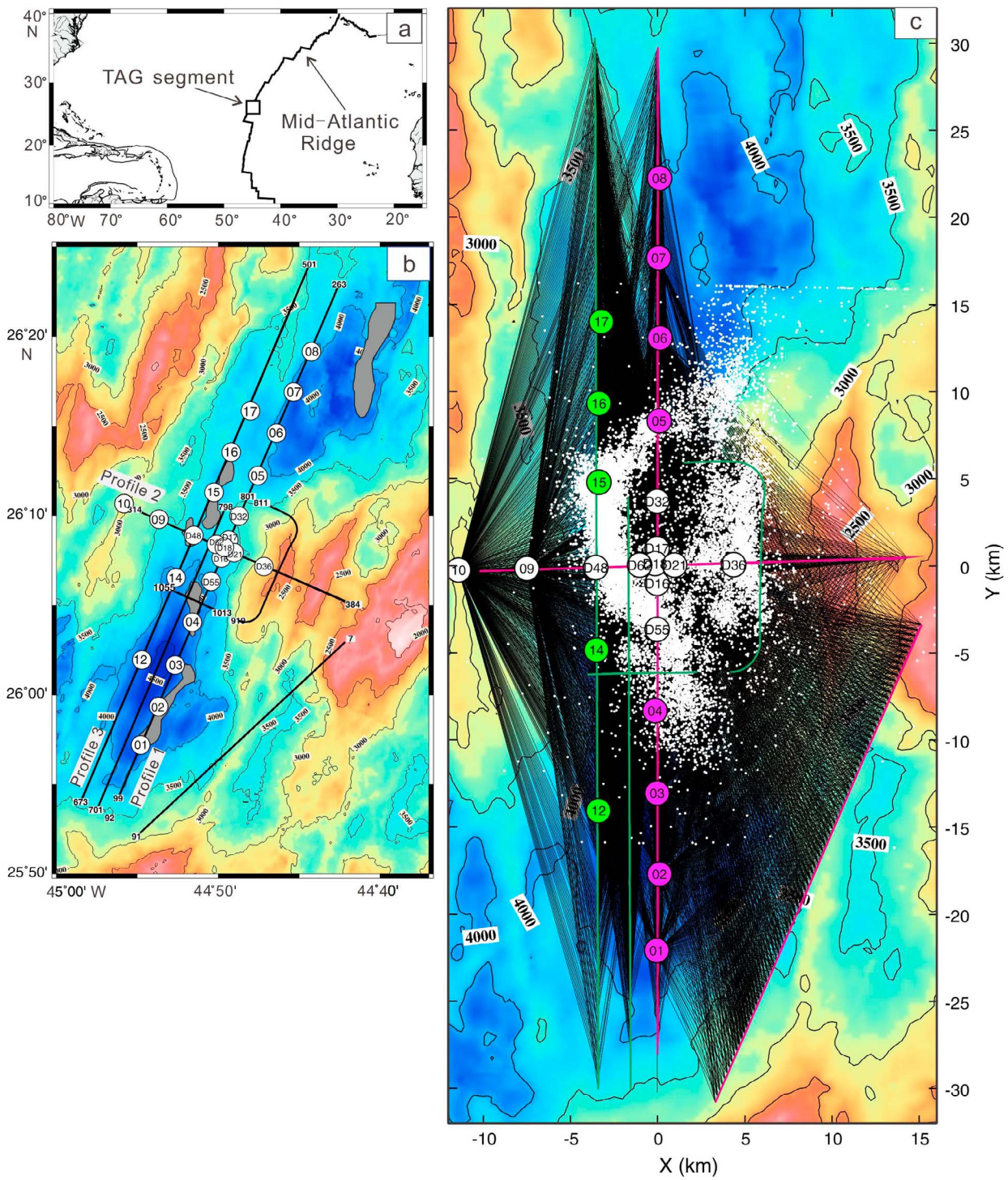

Figure 1. (a) Location of the TAG segment along the Mid-Atlantic Ridge. (b) Bathymetry map and OBS seismic survey. Bathymetry contours labeled every 500 m. Labeled white circles are OBSs. Thick lines represent air gun shooting profiles, with bold numbers indicating shot number at the beginning and end of the profiles. Shaded patches are neovolcanic zones. (c) Bathymetry map of the study area in Cartesian coordinates (origin of the local coordinate system corresponds to −44.82615°W, 26.13508°N; *y* axis is oriented 22 degrees clockwise from North). Magenta and green labeled circles correspond to OBSs that recorded air gun signals along profiles displayed with the same color. The OBSs shown as white circles recorded all air gun signals. White dots are microearthquake epicenters from the catalog of *deMartin et al.* [2007]. Black lines connect all of the source-receiver pairs for which travel-times were picked and used in the tomography inversion.

1986, 1984]. One of them – the active TAG mound – is presently discharging fluids at temperatures of up to 360°C [*Sohn*, 2007].

[8] Hydrothermal discharge has been occurring in this area for at least the past ∼150 kyr [*Lalou et al.*, 1995], generating ∼3.9 million tons of massive sulphide deposits [*Humphris et al.*, 1995]. Vent fluid composition at TAG is generally similar to that of fluids sampled at the fast spreading East Pacific Rise [*Campbell et al.*, 1988; *Edmonds et al.*, 1996], and the low fluid pH [*Campbell et al.*, 1988] suggests little interaction with ultramafic rocks. However, the presence of native Ni particles in sediments nearby have been interpreted as being derived from tectonically uplifted serpentinized ultramafics/mafics [*Dekov*, 2006], and low boron levels in TAG fluids have likewise been interpreted to result from boron removal during the serpentinization of ultra-mafic rocks [*Palmer*, 1996]. Sr and O isotopes in fluid samples indicate that flow pathways in this system are longer, and probably penetrate deeper, than in other hydrothermal systems hosted in fast spreading MORs [*Bach and Humphris*, 1999].

[9] The eastern valley wall comprises sedimented, uplifted, terraces and fault scarps [*Kleinrock and Humphris*, 1996] that in some instances expose gabbros [*Zonenshain et al.*, 1989], indicating exposure of intrusive crustal rocks there. *Tivey et al.* [2003] argue that a low magnetization anomaly observed along the eastern valley wall is consistent with ∼4 km of extension along a detachment fault since ∼0.35 Ma. These authors suggest that the active TAG hydrothermal mound is located on the hanging wall of a detachment fault, about 2.5 km away from the fault termination. Slip along the fault may have episodically increased the permeability of the hanging wall, reactivating the overlying hydrothermal systems and contributing to their longevity [*Tivey et al.*, 2003].

2.2. Previous Seismic Studies

[10] An early microseismicity and controlled-source seismic study of the TAG segment using seven ocean bottom hydrophones and three OBSs [*Kong*, 1990; *Kong et al.*, 1992] reported high levels of seismicity during a three-week period in 1985 along the median valley floor with hypocentral depths ranging between 3 and 7 km bsf (with earthquake depth generally increasing away from the segment center). *Kong et al.* [1992] also reported the presence of a low *P*-wave velocity zone at a depth of 3–6 km beneath the neovolcanic zone at 26°06′N that was interpreted as a recent magmatic intrusion.

[11] More recently, the STAG experiment recorded microseismicity at the TAG segment during an 8-month period in 2003 using a network of 13 OBSs [*deMartin et al.*, 2007]. Hypocenters from nearly 20,000 microearthquakes with local magnitudes between $1 \leq M_L \leq 4$ define a ∼15-km-long, steeply dipping (∼70°), arcuate fault surface that penetrates to depths >7 km bsf [*deMartin et al.*, 2007].

[12] The STAG experiment included a controlled-source wide-angle OBS experiment to determine the crustal architecture of the TAG segment [*Canales et al.*, 2007; *deMartin et al.*, 2007]. Two-dimensional *P*-wave velocity models revealed a pronounced asymmetry across the rift valley floor. Velocities greater than 6.5 km/s at depths as shallow as 1 km bsf were found along the eastern valley wall, forming a roughly triangular shaped (in the along-axis direction) high-velocity body centered at the segment center that was interpreted as the uplifted footwall of the detachment fault. The velocity contrast (6.5 km/s immediately overlain by ∼4.0 km/s) interpreted as the hanging wall/footwall interface dips at ∼20° toward the ridge axis within the upper ∼3 km of the velocity model, which contrasts with the 70° dip of the fault interface as inferred from the microearthquake hypocenters at depths greater than 3 km, suggesting that the detachment originates at high angles and undergoes significant flexural rotation to low angles as the footwall is exhumed [*Canales et al.*, 2007; *deMartin et al.*, 2007].

[13] Significantly, *Canales et al.* [2007] did not find evidence in the wide-angle refraction data for the mid-crustal low seismic anomaly reported by *Kong et al.* [1992], which was interpreted to as a hot but solidified recent magmatic intrusion. Instead, the deep penetration of the microearthquakes (>7 km bsf) indicates that the brittle lithosphere is relatively thick, which led *deMartin et al.* [2007] to hypothesize that hydrothermal fluids at TAG must be extracting heat from a deep (>7 km bsf) magmatic reservoir.

3. Three-Dimensional Seismic Tomography

3.1. Wide-Angle Seismic Data

[14] Details regarding the OBS recording parameters and source characteristics can be found in *Canales et al.* [2007], where the 2D crustal

structure along three profiles (two along-axis and one across-axis) is reported. The OBSs, however, also recorded air gun shots fired along auxiliary lines and transits between the main profiles, as well as arrivals from off-line shots (Figure 1). OBSs 01–08 recorded shots numbered 99–263 along the eastern side of the valley floor (Profile 1 in *Canales et al.* [2007]), shots 314–384 across the rift valley (Profile 2 in *Canales et al.* [2007]), and shots 7–91 across the southwestern flank of the segment. OBSs 12–17 recorded shots 501–673 (Profile 3 in *Canales et al.* [2007]) and shots 701–798 along the center of the valley floor, and shots 801–1055 along roughly circular line centered at the active TAG mound. OBSs 09, 10, and OBSs D16–D62 recorded all of the shots fired during the experiment. Adding these arrivals results in a total of 8,982 high-quality travel-time picks, which is significantly larger than the 2,656 source-receiver pairs used in the 2D analyses. By adding these off-line raypaths to the analysis we achieve dense ray coverage with a broad range of azimuths at the center of the segment, particularly in the region characterized by microseismic activity related to detachment faulting (Figure 1c). These new data allow us to expand the 2D results from *Canales et al.* [2007] into a 3D seismic tomography model.

[15] *P*-wave first arrival travel times were hand-picked in band-pass filtered (5–20 Hz) record sections without differentiating between crustal (*Pg*) and mantle (*Pn*) refracted phases, and excluding direct water-wave arrivals (Figure 2). Observed travel-time uncertainties were calculated based on the signal-to-noise ratio (SNR) [*Zelt and Forsyth*, 1994]. SNR was calculated as the square root of the ratio between maximum trace amplitudes in a 250-ms window before and after pick. In addition, travel time uncertainties included a constant value of 30 ms to account for uncertainties in source and receiver location and uncertainty in seafloor ray entry point in areas with large topographic variations.

3.2. Tomography Method

[16] We applied the iterative first-arrival tomography method of *Zelt and Barton* [1998] to obtain a smooth, isotropic 3D *P*-wave velocity model of the TAG segment. We seek a solution with the least amount of required structure that fits the observed data adequately (ideally with a normalized χ^2 misfit as close as possible to 1). This is accomplished by using a regularized least squares solution to the inverse problem that minimizes an objective function that includes the data residuals (weighted by their uncertainty) and the second spatial derivative of the model parameters [*Zelt and Barton*, 1998]. The tradeoff between minimizing travel-time residuals and obtaining a smooth solution is controlled by the parameter λ. We run a number of inversions to find the appropriate values of λ and the horizontal grid node spacing for the inverse problem (D_{xy}). The forward problem (raypath and travel time calculations) is solved on a volume with a uniform node spacing of 250 m in X, Y, and Z directions. Ray entry points in the seafloor are found along 3D raypaths with minimum travel time between sources and receivers. A relatively dense parameterization of 113 × 257 horizontal nodes in an area of 28 km × 64 km and 53 vertical nodes from 0 to 13 km below the seafloor (1,539,173 nodes in total) is used for ray tracing. The inverse problem uses a volume with 1000 m cell spacing of both horizontal directions and 500 m in the vertical direction (46,592 cells in total). The seafloor interface was constructed from multibeam bathymetry data acquired during the STAG experiment. Velocity in the water layer was fixed at 1.5 km/s.

[17] For this set of inversions we used the one-dimensional (1D) average velocity model of Profile 1 of *Canales et al.* [2007, Figure 4] as our starting model. The 1D structure was draped from the seafloor to build the starting 3D volume. Travel-times predicted by this 1D structure fit the data poorly ($\chi^2 > 24$; Figures 3a and 3b) with residuals ranging from −400 to 500 ms, indicating that a simple 1D structure cannot satisfactorily explain the observed data. We explored solutions in this two-parameter space for λ values between 1 and 10, and D_{xy} values between 500 and 5,000 m. Results show that the combination (λ = 1 and D_{xy} = 1,000 m) provides the best fit to the data (χ^2 = 1.7 in Figure 4).

3.3. Preferred *P*-wave Velocity Model and Data Fit

[18] Any solution to the inverse problem depends to some degree on the starting model chosen. To account for the influence of the starting model on the solution and to obtain an estimate of the uncertainty that the starting model introduces in the final solution, we followed a Monte Carlo approach similar to that of *Zhang et al.* [1998] and *Korenaga et al.* [2000]. We constructed 100 random 1D initial models (Figure S1 in the auxiliary material) and ran 100 different inversions.[1] Assuming that the

[1]Auxiliary materials are available in the HTML. doi:10.1029/2012GC004454.

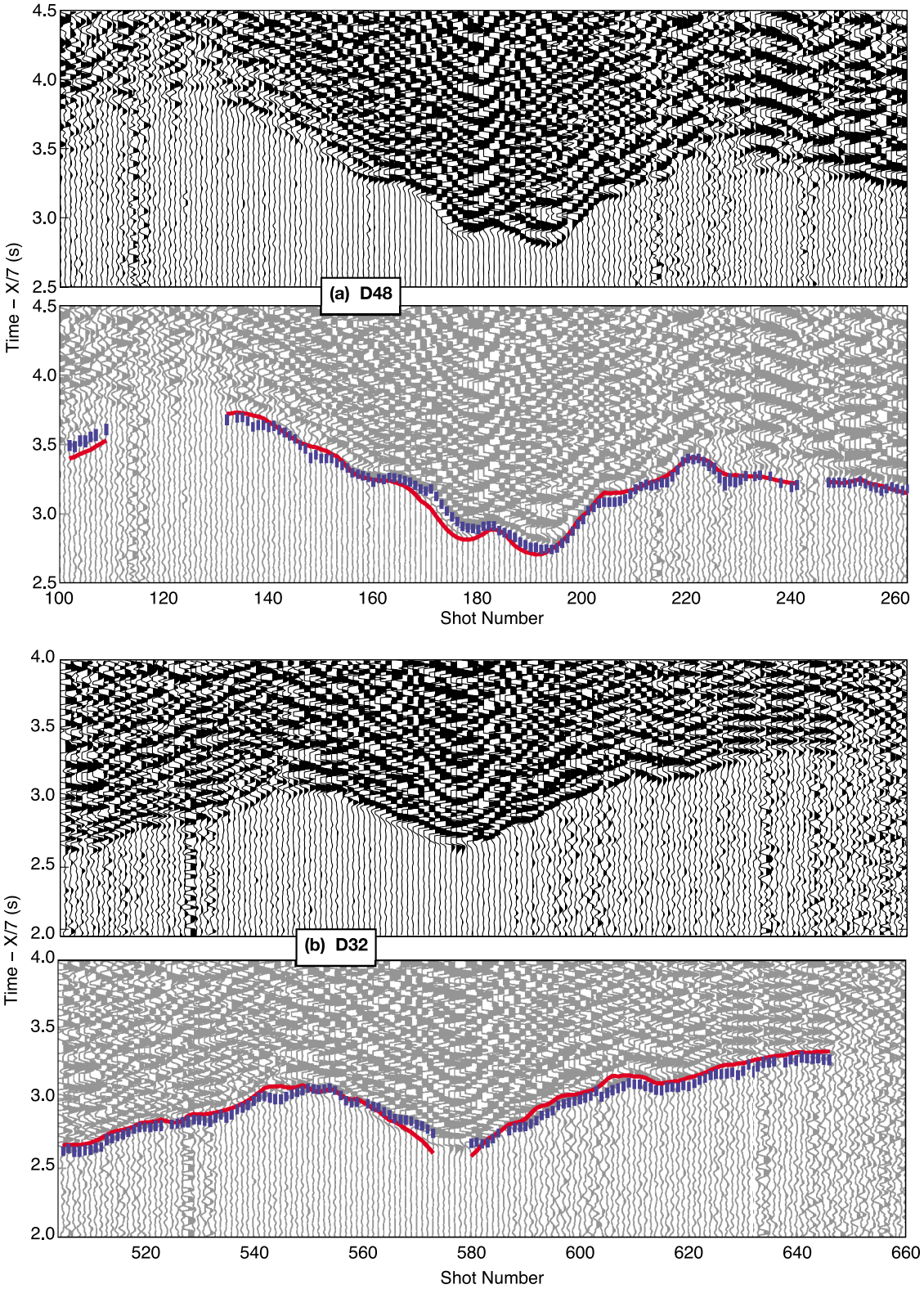

Figure 2. Examples of two seismic record sections for instruments (a) D48 and (b) D32 showing off-line recordings. Data have been band-pass filtered between 5 and 20 Hz, and amplitudes have been scaled according to range for display purposes. Bottom panels show observed travel-time picks (blue vertical bars with length equal to the assigned travel-time uncertainty) and calculated travel times (the red line) predicted by the final model.

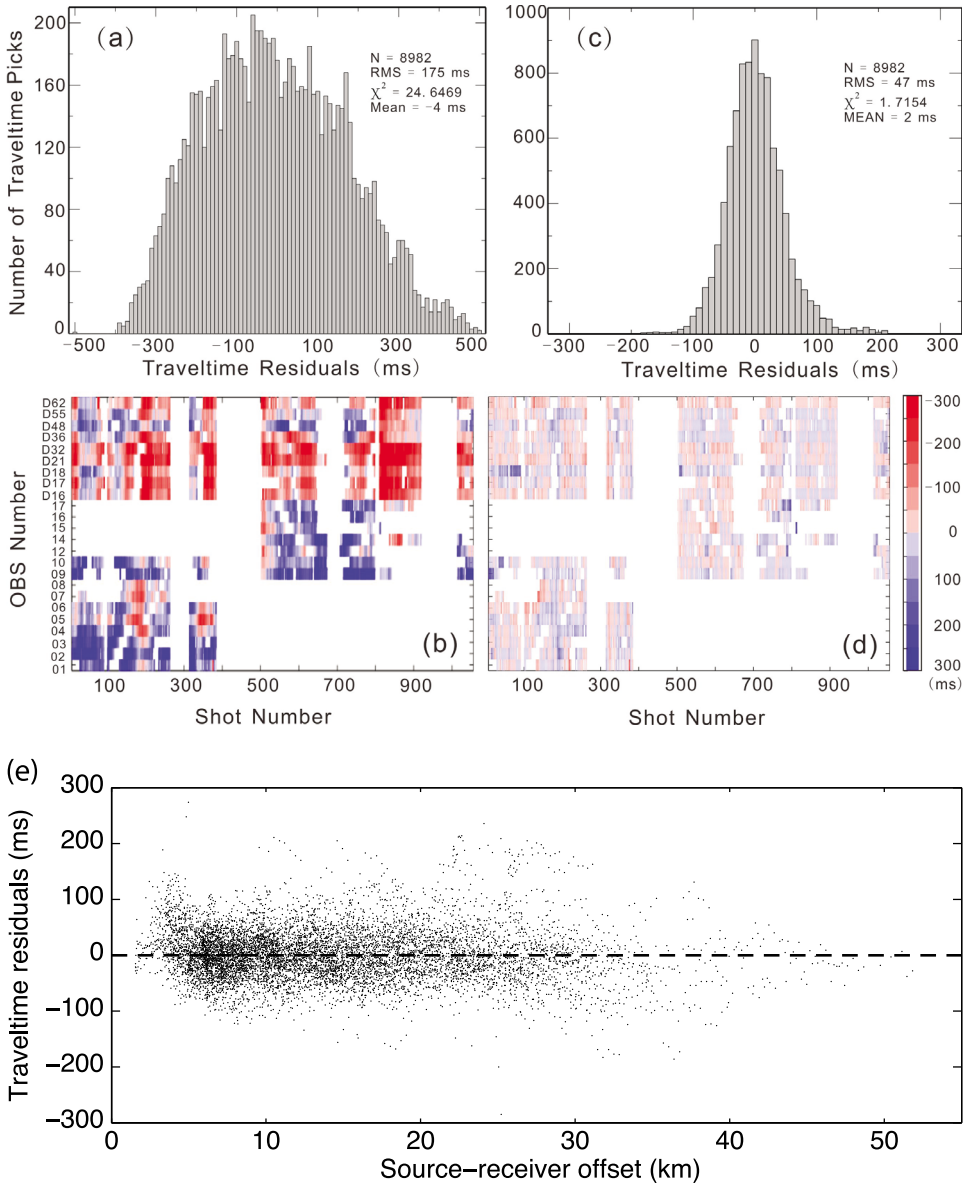

Figure 3. Histograms of traveltime residuals calculated by (a) the starting 1D model and (c) the final model. (b and d) Color maps of traveltime residuals as a function of shot number and source, predicted by the starting 1D model before inversion and by the final model, respectively. The vertical axis indicates the OBS numbers, color scale indicates the traveltime residuals for each shot. (e) Traveltime residuals of the preferred velocity model as a function of source-receiver offset.

random initial models are not correlated among each other and that all solutions are equally valid, the average ensemble and the standard deviation of the 100 solutions are valid statistical estimates of the final model and its uncertainty [e.g., *Korenaga et al.*, 2000].

[19] The 100 inversions were run using the parameters described in the previous section. The preferred velocity model (Figure 5) was constructed by averaging the 100 inverse solutions, and it predicts travel-time residuals that are normally distributed with χ^2 = 1.72 (Figure 3c). All instruments are equally well fit, with no travel-time residual dependence on shot number or instrument location (Figure 3d). Data residuals do not show dependence with source-receiver offset, indicating that observations are equally well fit at all offsets (Figure 3e). Travel-time residuals do not have a resolvable dependence with source-receiver azimuth, even when residuals are binned according to ray turning depth. Thus, even if our solution is isotropic, we cannot detect any anisotropic signature in the data

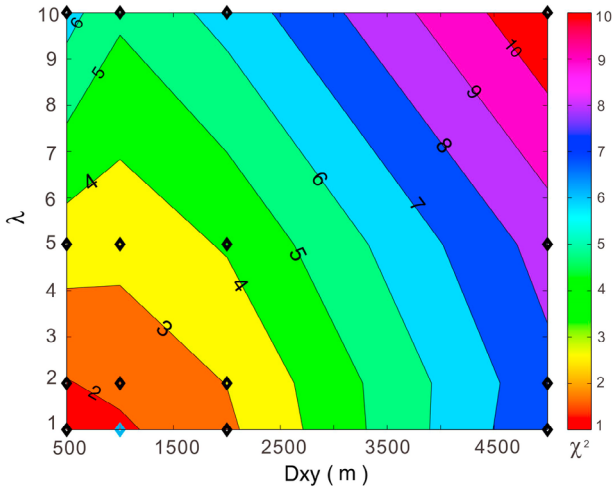

Figure 4. Contour plots of the traveltime misfit function χ^2 as a function of λ and the horizontal correlation length D_{xy}. Black diamonds show the pair combinations tested. Blue diamond corresponds to the parameters used in the preferred inversions in our modeling.

residuals as has been shown before in other MOR settings [*Dunn and Toomey*, 2001; *Dunn et al.*, 2005; *Sohn et al.*, 1997].

3.4. Velocity Model Description

[20] The preferred model confirms the main features reported by *Canales et al.* [2007], such as the asymmetric seismic structure of the TAG segment (Figure 5b, Y = 0 km) and the triangular, or dome-shaped high-velocity body at the center of the segment (Figure 5a, X = 0 km). However, the larger data set and wider azimuthal coverage employed here allows a better characterization of these features, in particular their spatial variation both along- and across-strike. Estimates of the model uncertainty (Figure S2) and checkerboard resolution tests (Figure S3) are described in the auxiliary material.

[21] In an across-axis section the TAG segment exhibits an asymmetric structure (Figure 5b), with the eastern valley wall and ridge flank characterized by elevated seismic velocities (>6 km/s), within the upper 1 km of crust. In contrast, velocities of 6 km/s or higher beneath the western side of the rift valley are only found at sub-seafloor depths greater than 2 km. This asymmetric pattern results from a high-velocity region that occupies the central part of the segment, with an across-axis width of ~12 km from X ≈ −2 km to X ≈ 10 km (Figures 5b and 5c). In the along-axis direction, this high-velocity region has a triangular shape with a length of ~10 km at 2 km bsf and ~20 km at 4 km bsf (Figures 5a and 5c).

[22] In plan view, the high-velocity region at shallow depths (e.g., Z = 1 km bsf, Figures 6a, 6b, and 7) is bounded by the deeper local microseismicity, reinforcing the interpretation of *deMartin et al.* [2007] and *Canales et al.* [2007] that this feature represents the uplifted footwall of the TAG detachment fault. As depth increases, the velocity structure of the footwall becomes more heterogeneous, with the southern half of the footwall showing lower velocities than the northern half (Figures 6c and 6d) (i.e., 6.5 km/s versus 7.0 km/s at sub-seafloor depths >2 km, Figures 5c and 7). At shallow levels (2 km bsf), this relative low velocity zone (6.2–6.5 km/s) is surrounded by high-velocity zones (>7 km/s) to the north, south, and east, and a lower velocity region outboard of the detachment fault to the west (Figure 6). At greater depths, the low velocity zone becomes wider, eventually occupying all except the northwestern corner of the footwall at 4 km bsf (Figure 6). The footwall low velocity zone is in most parts also coincident with a velocity inversion occurring at ~1.5 km bsf (Figure 7). The velocity inversion, which is defined by a pronounced negative vertical velocity gradient, occupies a ~5-km-wide zone extending from just southwest of the TAG active hydrothermal mound to the central-eastern edge of the footwall (Figure 8).

4. Observation and Modeling of Shallow Crustal Reflections

[23] *DeMartin et al.* [2007] interpreted the steep dip of the TAG microearthquakes and the asymmetric crustal structure revealed by seismic refraction data as resulting from a single detachment fault that rotates ~50° in the upper crust. Although this interpretation is consistent with other geophysical and geological observations [e.g., *Tivey et al.*, 2003; *Zonenshain et al.*, 1989], the shallow-dipping fault zone in the shallow crust has yet to be directly imaged. To this end we use forward modeling to compute synthetic seismograms to aid identification of arrivals in the OBS refraction data that might represent reflections from a fault interface in the shallow crust.

4.1. Forward Modeling of Synthetic Seismograms

[24] We calculate seismograms simulating the OBS data from Profile 2 (Figure 1) using two different

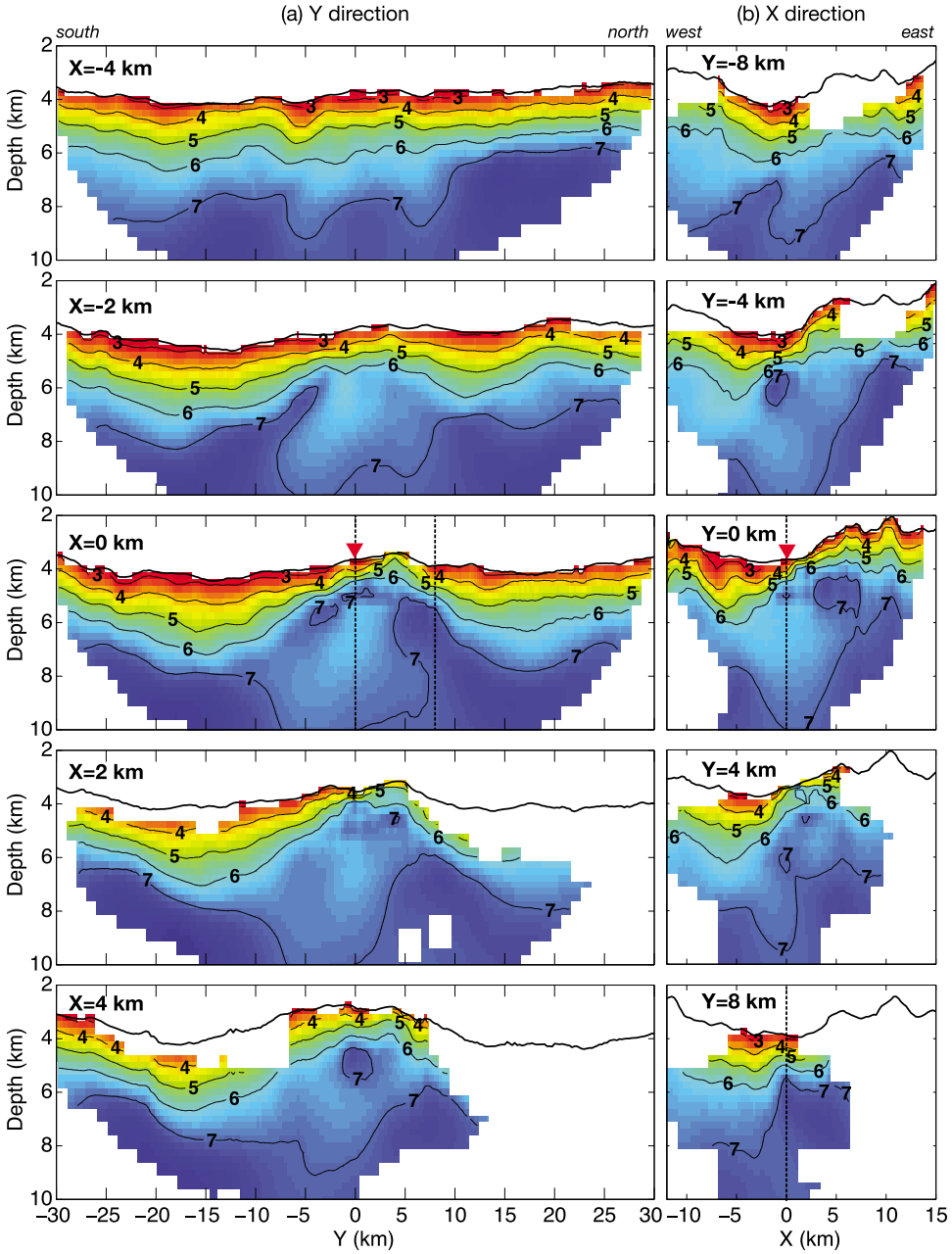

Figure 5. Vertical and horizontal sections from the final velocity 3D model. Masked (white) regions correspond to lack of ray coverage. (a) Cross-sections along the Y direction are at $X = -4$, -2, 0, 2, and 4 km. (b) Cross-sections along the X direction at $Y = -8$, -4, 0, 4, and 8, km. (c) Map-view slices are at sub-seafloor depths of 0.5, 1.0, 2.0, and 4.0 km. Contours in Figures 5a and 5b every 1 km/s, and in Figure 5c every 0.5 km/s. Vertical dashed lines in Figures 5a and 5b show locations of the velocity-depth functions shown in Figure 7. Red triangles in Figures 5a and 5b indicate the location of the TAG active hydrothermal mound. Shaded areas in Figure 5c are neovolcanic zones.

velocity models: a model based on the velocity structure of Profile 2 that we name "no fault model" (Figure 9a), and a second model named "detachment fault model" (Figure 9b) in which we have introduced a 100-m-thick low-velocity (3 km/s) fault zone [e.g., *MacLeod et al.*, 2002] mimicking the inferred fault geometry across the rift valley of *deMartin et al.* [2007]: 70° dip in the lower section and 20° dip in the shallow part of the fault zone, and assuming that the fault breaks the seafloor at X = 2 km (Figure 9b).

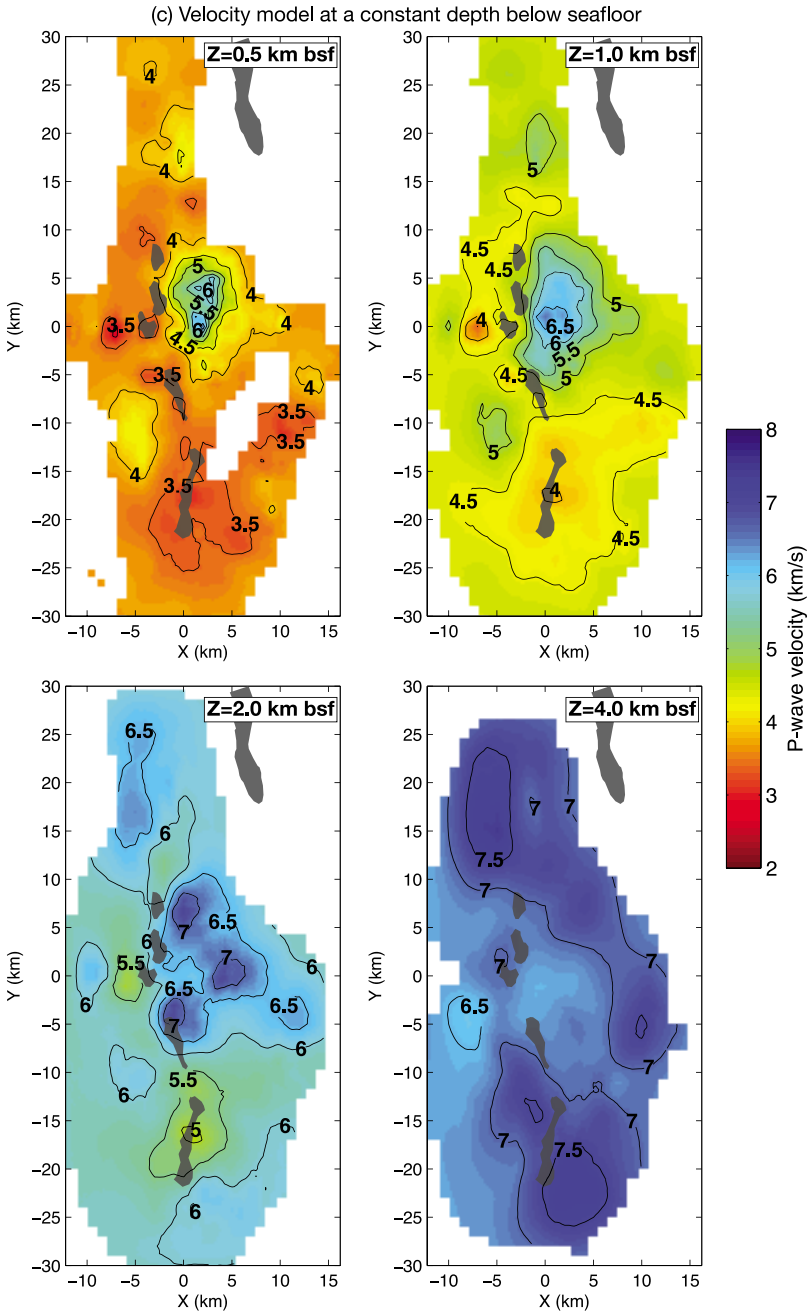

Figure 5. (continued)

[25] Synthetic seismograms were calculated using a finite difference approximation of the acoustic wave equation in the frequency domain [*Pratt*, 1999]. *P*-wave velocity, density and attenuation were defined in 3601 × 801-node regular grids with 12.5 m node spacing. Densities were estimated from the *P*-wave velocities using the relationships of *Carlson and Raskin* [1984], and attenuation was set to $Q_p^{-1} = 10^{-4}$ in the water layer and $Q_p^{-1} = 10^{-3}$ below the seafloor. The source is a three-excursion Kupper wavelet with a central frequency of 11.8 Hz. Synthetic seismograms were calculated for 540 frequency components evenly distributed between 0 and 45 Hz. The numerical simulations indicate that reflections from the fault should be best observed at source-receiver offsets <4 km, a few to several hundred (~200–1,000) milliseconds behind the direct water wave (Figures 9d–9g).

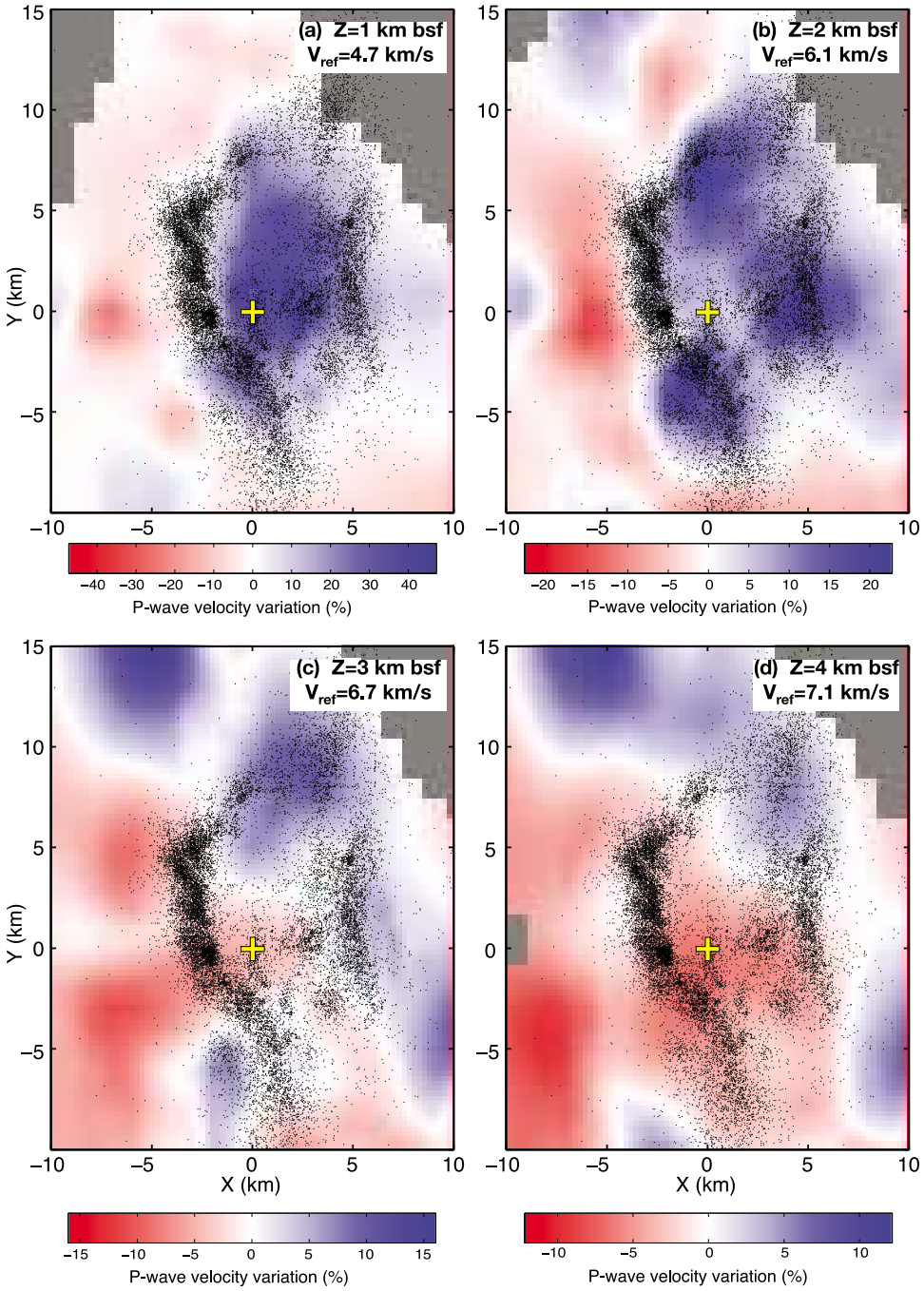

Figure 6. Horizontal sections from the central part of the final velocity 3D model at sub-seafloor depths of (a) Z = 1 km bsf; (b) Z = 2 km bsf; (c) Z = 3 km bsf; and (d) Z = 4 km bsf. The model is shown as percentage of variation in *P*-wave velocity from the mean velocity V_{ref} at each depth. Also shown are hypocenters from the catalog of *deMartin et al.* [2007] (dots) and the location of the TAG active hydrothermal mound (yellow cross).

4.2. Seismic Reflections in the OBS Data Set

[26] Based on the forward modeling results we inspected data recorded along the across-axis Profile 2, focusing on the near offsets in a narrow time window immediately after the arrival of the direct water wave (Figure 9c). Data from instruments D35 and D21 show seismic arrivals with characteristics similar to those predicted by the "detachment fault model" (Figures 9d and 9e), while the data from instrument D62 is somewhat equivocal (Figure 9f).

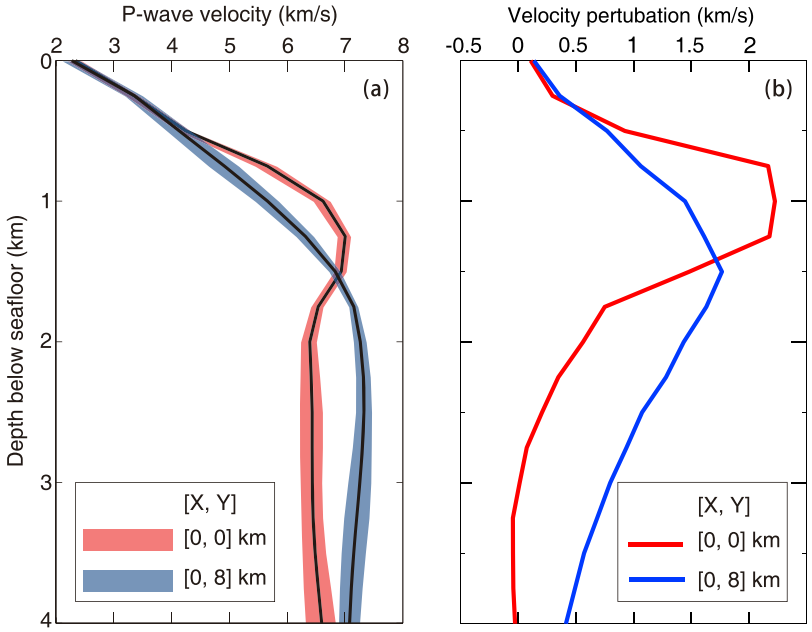

Figure 7. Comparison of 1D velocity-depth profiles extracted from the preferred model. The shaded areas indicate $\pm 1\sigma$ velocity uncertainty. (a) Absolute V_P. (b) Relative variation in V_P with respect to the starting 1D model.

In contrast, data from instruments D48, 09, and 10 do not show any evidence of shallow crustal reflections (Figures 9g and 10).

[27] We have employed a relatively simple approach in order to investigate the feasibility of observing reflections from a low-angle fault in the shallow crust within our study area. We have found that several of our instruments exhibit reflected arrivals in the time windows expected for our assumed fault geometry, although we acknowledge that our simple model cannot fully describe the data. For example, data from OBS D36 show arrivals from a shallow reflector at 0–3 km offset (Figure 10) that were not predicted by our model (because of the position of the instrument relative to the fault), which may indicate that the fault geometry is different or more complex than assumed in our model. More sophisticated models could be generated (e.g., modifying the velocity and fault geometry of the "detachment fault model") with the aim of inferring the fault geometry from ray-tracing and travel-time modeling, but the data from the OBS network is too sparse to support such analyses. A dedicated seismic reflection survey employing a streamer and/or a denser network of OBSs and closely spaced shots will be required to fully constraint the geometry and nature of the shallow reflector evidenced in our records. In Section 5.2 we discuss possible origin(s) for the observed seismic arrivals, and consider the

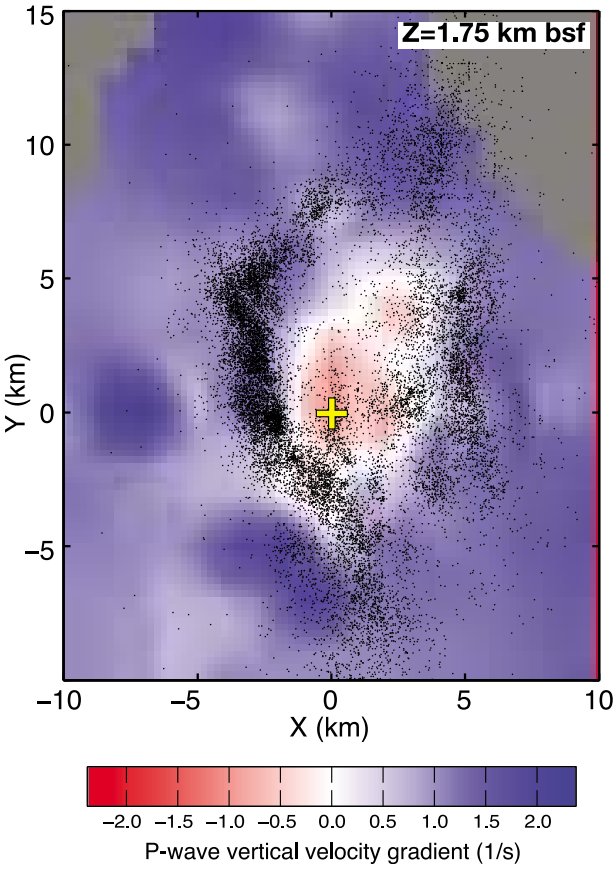

Figure 8. Vertical velocity gradient of the final velocity 3D model at a depth of 1.75 km bsf. Dots are hypocenters from the catalog of *deMartin et al.* [2007].

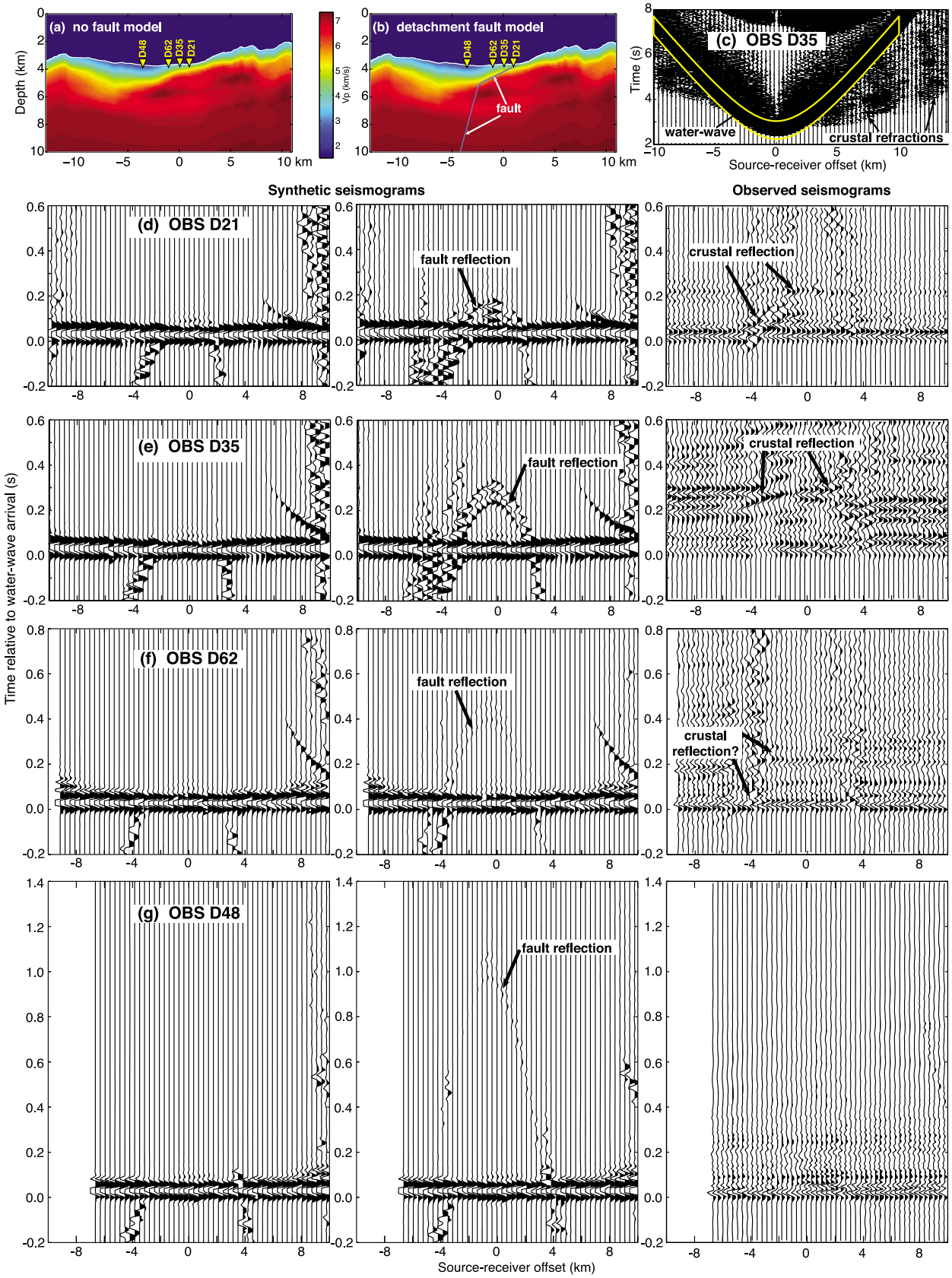
(a) no fault model
D48
D62
D35
D21
Depth (km)
Vp (km/s)
(b) detachment fault model
fault
10 km
(c) OBS D35
Time (s)
water-wave
crustal refractions
Source-receiver offset (km)
Synthetic seismograms
Observed seismograms
(d) OBS D21
fault reflection
crustal reflection
(e) OBS D35
(f) OBS D62
crustal reflection?
(g) OBS D48
Time relative to water-wave arrival (s)
Source-receiver offset (km)

Figure 9

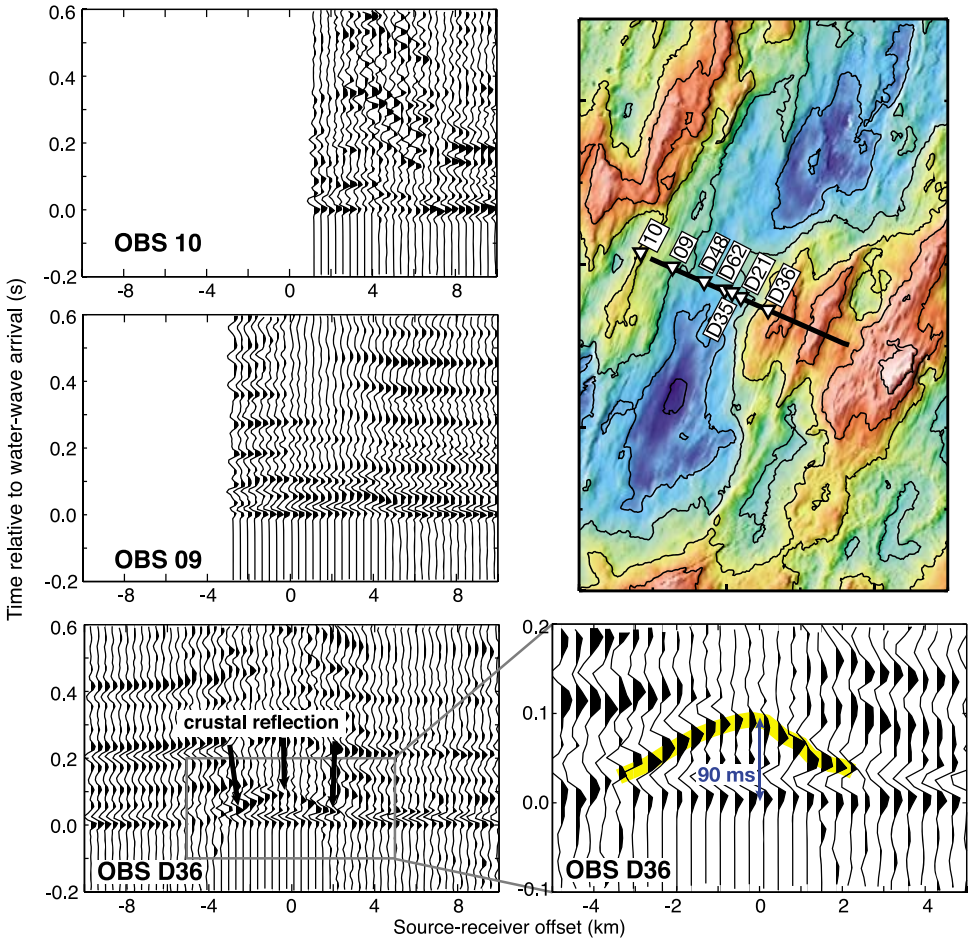

Figure 10. Observed record sections (plotted in the same time-offset window as those from Figure 9) for other instruments located along Profile 2 (location shown on top-left bathymetry map).

implications of the shallowly dipping fault zone hypothesis.

5. Discussion

5.1. Implications for the Timing and Longevity of Detachment Faulting at TAG

[28] Based on a near-bottom magnetic study, *Tivey et al.* [2003] proposed that the TAG ODF is an incipient feature that has been active since ~0.35 Ma, in which case exhumed footwall rocks should only be present within a ~4-km-wide region just east of the TAG active hydrothermal mound. In contrast, *Smith et al.* [2008] and *Schouten et al.* [2010] propose that detachment faulting has been occurring on the east flank of the TAG segment for at least the last 2 My based on the morphological characteristics of a series of lineated ridges on the eastern ridge flank interpreted to be rafted hanging wall blocks. Our new 3D velocity model of the TAG segment is more consistent with the hypothesis of *Smith et al.* [2008] because we find that the asymmetric velocity structure characterized by high *P*-wave velocity in the eastern flank extends at least 15 km east of the present spreading axis (Figure 5).

Figure 9. Velocity model along Profile 2 (Y = 0 km): (a) "no fault model" [*Canales et al.*, 2007] and (b) "detachment fault model," after introducing a 100-m-thick low velocity zone simulating the TAG ODF. (c) Record section for OBS D35 for shots along Profile 2. The hyperbolic yellow box around the direct water wave arrival indicates the time window shown in Figures 9d–9g, both for the synthetic and observed seismograms. (d–g) Observed (right) and synthetic (middle, left) seismograms computed using the "no fault model" (left) and the "detachment fault model" (middle) velocity models.

(We consider that the spreading axis is defined by the neovolcanic zones, which are located at X = −4 km for Y = 0 km, and that good model resolution at Y = 0 km is limited to the region where X < 10 km, Figure 6). If we assume symmetric spreading and a total spreading rate of 22 km/Myr [*Tivey et al.*, 2003], our results suggest that detachment faulting has been active at TAG at least for the last ∼1.35 Myr. However, detachment faulting may be associated with asymmetric accretion [e.g., *Okino et al.*, 2004; *MacLeod et al.*, 2009], accommodating perhaps up to 80% of the plate separation [*Baines et al.*, 2008], such that our estimate may represent an upper bound. Furthermore, we note that our data and models cannot discern whether extension has occurred on a single long-lived detachment fault as opposed to a series of consecutive, shorter-lived, detachment faults.

5.2. New Constraints on the Geometry of the TAG Detachment Fault

[29] The reflections we observed in some of the STAG record sections (Figures 9 and 10) are generated by impedance contrasts in the shallow crust, but the reflections themselves are not diagnostic of the source zone lithologies. The two most geologically probable reflectors are a low-angle fault zone (as per our synthetic models) and the transition from extrusive to intrusive basalt lithologies (i.e., seismic layer 2A/2B interface). Reflections from the seismic layer 2A/2B interface have been observed at other MAR segments, and the timing of these arrivals (e.g., 0.2–0.4 s below the seafloor at segment OH-1 near 35°N [*Hussenoeder et al.*, 2002] and ∼0.4–0.6 s bsf at the Lucky Strike segment [*Seher et al.*, 2010a]), are consistent with the reflector travel-times observed in the STAG data set (Figures 9 and 10). Therefore we cannot rule out the possibility that the reflections we observe correspond to the seismic 2A/2B boundary. However, given that the TAG segment is known to host an active oceanic detachment fault, and that the observed arrivals are qualitatively similar to those predicted by a model with a low-angle fault in the shallow crust (Figure 9b), we prefer the low-angle fault zone model for our observations.

[30] If our interpretation is correct, then the observation of shallow reflected arrivals at OBS D36 (Figure 10) suggests that the shallow portion of the fault may extend farther east than previously supposed. This supports the idea that the linear ridges forming the east flank of the TAG segment are tilted drafted blocks that cap the TAG OCC [*Smith et al.*, 2008], a style of detachment faulting that is proposed to occur preferentially near segment centers [*Reston and Ranero*, 2011], as it does here. We can use the timing of zero-offset (i.e., when the air gun source is directly above an OBS on the seafloor) reflected arrivals to constrain the subseafloor depth of the source reflector beneath OBS D36. This instrument shows zero-offset reflections ∼90 ms behind the direct water wave (Figure 10), corresponding to a source depth of ∼150 m bsf (assuming shallow crustal velocities of ∼2400 m/s). This estimate is likely a maximum value because shallow crustal velocities tend to be overestimated in wide-angle velocity models. We do not consider the data quality for the reflections observed on OBSs D21, D35, and D62 to be sufficient to allow for arrival time picking, but it is nevertheless clear that the data trend toward later arrival times moving west across the profile, which also supports the idea of a westward dipping fault interface.

5.3. Footwall Structure and Hydrothermal Convection

[31] Early studies hypothesized that heat extracted from cooling hot but solidified mid-crustal plutonic intrusions is the main driver of high-temperature hydrothermal convention at the TAG segment [*Kong et al.*, 1992; *Rona et al.*, 1993; *Tivey et al.*, 2003] (although energy and chemical balances seem to require heat from crystallization of a melt reservoir [*Humphris and Cann*, 2000]). These ideas were modified in light of the results from the STAG experiment, wherein microseismicity was found to extend deep into the crust/uppermost mantle (>7 km) [*deMartin et al.*, 2007], and no evidence for a mid-crustal magma chamber (i.e., low-velocity anomaly) beneath the valley floor neovolcanic zones was found in the seismic refraction data [*Canales et al.*, 2007]. These results led to the hypothesis that the heat driving hydrothermal convection is sourced out of a magma body at the root zone of the detachment fault, in the lower crust/upper mantle.

[32] Our 3D tomographic velocity model contains a relatively low velocity anomaly (6.2–6.5 km/s) embedded within the high-velocity body forming the footwall of the detachment fault (Figures 5, 6, and 7). This feature extends from 1.5 km bsf to at least 4 km bsf (Figures 6 and 7). The low-velocity feature was recognized by *Canales et al.* [2007] in their 2D model of Profile 1, but the new 3D model provides better constraints on its location and lateral extent. The velocity anomaly is centered beneath the

active TAG hydrothermal mound (Figure 6), and is surrounded by high-velocity zones where *P*-waves travel at 7.0–7.2 km/s (Figures 5c, 6, and 7). At greater depths, the low velocity anomaly becomes wider, about 8 km in diameter, eventually occupying most of the footwall at 4 km bsf (Figure 6), but its lowest value remains centered beneath the TAG hydrothermal mound ([X, Y] = [0, 0] km). Relatively low velocities are also present outside of the detachment footwall (e.g., along the valley floor, $X < -4$ km, and $Y < 10$ km, Figure 6), indicating that some caution is required when interpreting the low-velocity feature in terms of processes associated with the detachment footwall. However, a negative velocity gradient (i.e., velocity inversion, Figure 7) at a depth of ~1.75 km bsf overlies most of the low-velocity region, and it is spatially restricted to central and southern parts of the footwall (Figure 8). The region of velocity inversion is located beneath the TAG active hydrothermal mound, extending roughly SW-NE across a slightly elongated ~5 km × 8 km section of the footwall. Our resolution tests indicate that features of this size within this part of the 3D model are resolvable with our data (Figures S3g and S3h). The striking spatial correlation of this feature with the detachment footwall and the location of the active hydrothermal mound lead us to conclude that the velocity inversion and low-velocity anomaly underneath it are features associated with hydrothermal processes at TAG detachment fault system.

[33] We consider three possible scenarios for the origin of this region of anomalously low velocities: (1) a hot, perhaps partially molten, gabbro pluton intruding the detachment fault footwall; (2) serpentinized mafic/ultramafic rocks, with hydration of the footwall being enhanced by hydrothermal fluid flow; or (3) a highly fissured zone produced by extensional stresses during footwall exhumation.

5.3.1. Thermal/Melt Origin

[34] *Canales et al.* [2007] argued against a thermal source for the velocity anomaly based on thermal models of OCC formation [*Tucholke et al.*, 2008; *Williams et al.*, 2006], and the assumption that the observed seismic activity beneath the TAG active hydrothermal mound, which extends below ~5 km bsf, precludes the occurrence above this depth of temperatures higher than those associated with the brittle-plastic transition. These arguments remain valid, but they do not account for the complicated thermal structure of a detachment footwall that is likely to arise from the interplay of complex hydrothermal flow paths along the fault and within the footwall [*McCaig and Harris*, 2012; *McCaig et al.*, 2010], nor do they account for potential time-space variations in the emplacement of magma within the detachment fault system [*Olive et al.*, 2010]. Therefore we cannot rule out the possibility that the velocity anomaly (Figure 8) has a thermal origin possibly representing a hot, partially molten pluton. If this scenario is correct, then it may not be necessary to invoke deep heat extraction and along-fault fluid circulation for the TAG system [*deMartin et al.*, 2007]. A heat source located within the footwall could drive hydrothermal circulation at TAG and promote high-temperature alteration of footwall lithologies, as has been documented at Atlantis Massif OCC [*Nozaka and Fryer*, 2011].

5.3.2. Lithological Origin

[35] Geological and geophysical studies have documented the lithological heterogeneity of detachment fault footwalls, with gabbros and serpentinized peridotites being the dominant lithologies [e.g., *Blackman et al.*, 2011; *Canales et al.*, 2008; *Dick et al.*, 2008; *Henig et al.*, 2012; *Xu et al.*, 2009]. The footwall anomaly in our model has *P*-wave velocities in the range of 6.2–6.5 km/s, which are consistent with 50–60% serpentinized peridotite, while the high-velocity sections of the footwall (7.0–7.2 km/s) are consistent with either gabbro or 25–35% serpentinized peridotite [*Miller and Christensen*, 1997]. It is thus plausible that the velocity heterogeneity that we observe within the TAG footwall has a lithological origin, with the lower velocities corresponding to altered ultramafics and the higher velocities corresponding to gabbroic and/or less-altered ultramafic rocks. The velocity inversion (Figure 7) could thus represent a shallow gabbroic body overlying serpentinized peridotite. A similar velocity structure and stratigraphic relationship has been proposed for the Kane OCC [*Canales*, 2010], and is consistent with proposed models of OCC formation by intrusion of a gabbro body into a peridotite host [*Ildefonse et al.*, 2007].

[36] The arguments against the presence of altered ultramafics lithologies within the TAG footwall come primarily from the lack of observations of ultramafic exposures in the area [*Zonenshain et al.*, 1989], and from the chemistry of hydrothermal plume fluids [e.g., *Charlou et al.*, 1991]. The ratio of Total Dissolved Manganese (TDM) to methane (CH_4) concentration in fluids sampled from the water column above the TAG segment indicate that present-day hydrothermal fluids principally interact with basalt as opposed to peridotite [*Campbell et al.*,

1988; *Charlou and Donval*, 1993]. However, native Ni^0 particles recovered from sediments surrounding the TAG hydrothermal field have been interpreted as resulting from the tectonic disturbance of a serpentinized fault zone [*Dekov*, 2006], and low boron levels in TAG fluids have been attributed to serpentinization in the downgoing convection limb [*Palmer*, 1996]. In addition, hydrothermal discharge at TAG has been episodic, with numerous periods of sporadic venting from the various mounds located on the detachment footwall over the past ~140,000 yrs [*Lalou et al.*, 1995, 1993], and we do not know how the fluid chemistry varied over this period. Thus it seems possible that previous episodes of hydrothermal discharge may have involved serpentinization of ultramafic rocks within the detachment fault zone, even though present-day fluids appears to react primarily with basalt.

5.3.3. Fracturing Origin

[37] The footwall of a detachment fault experiences bending stresses as it is exhumed and rotated to lower-angle dips in the shallow crust [*Buck*, 1988], and extension of the upper surface of the footwall has the potential to reduce seismic velocities via fracturing. This process would also increase permeability in the upper section of the footwall, which is likely to be exploited by circulating hydrothermal fluids. Fracturing of the footwall is thus a plausible hypothesis for the low velocity zone, but fracturing should be most intense in the region where the footwall is rotating, which is 2–3 km west of the active mound [*deMartin et al.*, 2007], and thus not co-located with the region of reduced velocities in our model. Also, this hypothesis would predict that bending-related fractures extend all the way up to the seafloor, which seems inconsistent with the velocity inversion (Figure 7).

[38] In summary, we cannot rule out any of the three potential mechanisms (i.e., thermal, serpentinization, fracturing) on the basis of the extant data, and a combination of any/all of them is also possible given the causal relationships between heat, permeability, and hydrothermal circulation. Regardless of the process responsible for generating the footwall velocity anomaly in our 3D model, it seems likely that the conceptual model of *deMartin et al.* [2007] and its generalization and broader implications put forth in *McCaig et al.* [2007] will need to be revised to include additional complexity in the detachment footwall. Additional research will be required to determine the mechanism(s) that have created the seismic velocity structure of the detachment footwall, and this is an important topic for future work at TAG.

5.4. Comparison With Other MAR Segments

[39] We compare our 3D velocity model for the TAG segment with results from other similar and contrasting MAR segments where seismic studies of comparable scale and resolution have been conducted: at 22°19′N where an OCC forms the western MAR flank [*Dannowski et al.*, 2010], and the magmatically robust segments OH-1 at 35°N [*Magde et al.*, 2000; *Dunn et al.*, 2005] and Lucky Strike at 37°20′N [*Seher et al.*, 2010b].

5.4.1. The OCC at the MAR 22°19′N

[40] The MAR segment between 22°05–25′N is characterized by a dome-shaped massif located ~10 km off-axis forming the western valley wall, interpreted as an OCC. Here a 2D wide-angle seismic profile across the OCC and MAR valley shows a pronounced structural asymmetry in the upper 3–4 km of the lithosphere, with the west flank and OCC having higher seismic velocities than the eastern flank [*Dannowski et al.*, 2010]. The structural asymmetry is very similar to that found across the TAG segment, indicating that at both locations lithospheric structure is strongly controlled by uplift of deep lithological units and OCC formation. Perhaps the main difference is that the OCC at 22°19′N is more developed and probably more mature than the TAG OCC, although whether or not detachment faulting at 22°19′N remains active is unclear [*Dannowski et al.*, 2010]. *Dannowski et al.* [2010] reported observations of *PmP* reflections from the Moho beneath the OCC, which they interpreted as indicating continuous magmatic accretion during OCC formation. In our TAG data set we do not observed *PmP* arrivals from beneath the footwall, perhaps because the impedance contrast at the Moho beneath the TAG OCC may be less developed than at 22°19′N because of the TAG OCC is younger and not fully formed yet.

[41] Crustal thickness differences between the 22°19′N OCC and its conjugate flank were interpreted as resulting from slip along the fault and OCC rotation [*Dannowski et al.*, 2010] and not necessarily from asymmetric crustal accretion as has been proposed for other OCCs [e.g., *Baines et al.*, 2008]. Lack of *PmP* observations in our TAG data set and insufficient data coverage on the conjugate western flank prevent us from quantifying the amount of crustal asymmetry at TAG and its origin.

5.4.2. Magmatically Robust Segments

[42] The Lucky Strike segment, located just south of the Azores hot spot, has a well-developed axial valley and rift faults characteristic of the MAR, but it hosts an unusually large central volcano, indicating a robust magma supply [e.g., *Langmuir et al.*, 1997]. Here, an upper crustal low velocity anomaly extends along most of the segment, and at the segment center a lower crustal velocity anomaly is present beneath the central volcano [*Seher et al.*, 2010b]. Segment OH-1 lacks a well-developed central volcano as Lucky Strike does, but this segment is also considered to be magmatically robust based on its morphological and geophysical characteristics [*Detrick et al.*, 1995; *Hooft et al.*, 2000]. Upper crustal structure at OH-1 is characterized by an elongated (in the along-axis direction) axial low velocity zone above a center-of-segment, mid-crustal low-velocity zone [*Magde et al.*, 2000]. The axial low velocity zone extends into the uppermost mantle, and it is accompanied by more than 2 km of crustal thickening [*Dunn et al.*, 2005]. The lower and mid-crustal anomalies at both Lucky Strike and OH-1 have been interpreted as resulting from elevated temperatures and possibly some partial melt [*Dunn et al.*, 2005; *Seher et al.*, 2010b], which are thought to arise from focused magmatic accretion at the center of the segment [e.g., *Magde and Sparks*, 1997]. Anomalies in the upper crust likely represent increased porosity in the axial valley caused by extrusive volcanics and ridge-parallel fractures and fissures [*Dunn et al.*, 2005; *Seher et al.*, 2010b].

[43] In contrast to these two magmatically robust MAR segments, our model of the crustal structure at TAG does not contain upper and mid-crustal features that could be attributed to focused magmatic accretion and/or upper crustal diking zone. The lowest crustal velocity we find at 4 km bsf is 6.5 km/s (near X = −8 km, Y = −5 km, Figure 5c). This value is comparable to the lowest velocity reported at similar depth in OH-1 (6.4 km/s [*Magde et al.*, 2000; *Dunn et al.*, 2005]), but it is located beneath the western valley walls, suggesting that it does not correspond to an accretionary center. The upper crust at TAG also lacks the elongated low velocity anomalies of Lucky Strike and OH-1. With the exception of the southernmost neovolcanic zone (X ≈ 0 km, Y ≈ [−13, −21] km), none of the other mapped neovolcanic zones overly a zone of marked low velocity anomalies (Figure 5c). These observations indicate that mid- and upper crustal magmatic accretion at TAG is not focused at the segment center as other magmatically robust MAR segments, but instead is probably more diffuse and distributed along the segment. The absence of a high-amplitude mantle Bouguer gravity anomaly at the TAG segment [*Fujimoto et al.*, 1996] also suggests that accretion is not focused at the segment center at lower crustal or mantle levels. Thus our results suggest that supply of magma to the crust at the TAG segment is more distributed along-axis compared to magmatically robust segments like Lucky Strike and OH-1. It is unknown at this time whether a distributed magma supply is a general feature of MOR segments characterized by detachment faulting, or if this is specific to the TAG segment. Additional studies of the crustal architecture of segments with active detachments will be needed to assess this issue.

6. Conclusions

[44] We have generated a 3D *P*-wave tomographic velocity model of the TAG segment of the MAR, which includes the TAG oceanic detachment fault. The model provides evidence for a velocity inversion at 1.5–2.0 km bsf beneath a region of the footwall that includes the active TAG hydrothermal mound. *P*-wave velocities remain low (∼6.2–6.5 km/s compared to surrounding areas ∼7.0–7.2 km/s) down to 3.5 km bsf. We cannot constrain the source of this velocity anomaly with our data, but it likely results from some combination of thermal, lithological, mechanical, and hydrothermal processes. All of these processes lead to the conclusion that hydrothermal fluids circulate through the detachment footwall immediately beneath the active TAG mound, which appears to require modification to the conceptual model for hydrothermal circulation at TAG put forth in *deMartin et al.* [2007] and its broader implications for the relationship between hydrothermal fluid flow and detachment faulting [*McCaig et al.*, 2007].

[45] Our 3D *P*-wave velocity model shows that the structural asymmetry associated with detachment faulting extends at least ∼15 km from the ridge axis beneath a series of lineated ridges on the eastern ridge flank, indicating that faulting and uplift of deep lithologies has been occurring at the TAG segment for at least the last ∼1.35 Myr. We also observe seismic arrivals from a shallow crustal reflector in some of the OBS record sections. Forward modeling of synthetic seismograms indicates that these reflections are consistent with a westward shallow-dipping fault surface capping the central part of high-velocity footwall. Our observations also suggest that the fault zone may extend to the

east beneath the volcanic blocks forming the eastern valley wall. Our inferred age for the TAG ODF as well as the eastward extension of the presumed shallow fault zone are both consistent with generalized models of detachment faulting that propose that OCCs are more widespread than what can be inferred from seafloor mapping because OCCs are often buried beneath rafted hanging wall blocks [*Smith et al.*, 2008; *Reston and Ranero*, 2011].

[46] Outside of the TAG OCC, there is no evidence for upper or mid-crustal low velocity anomalies beneath the rift valley floor indicative of focused magmatic accretion, as is common in other magmatically robust MAR segments. This observation leads us to hypothesize that detachment faulting may develop in segments where melt supply is not focused at segment centers but more evenly distributed along the segment.

Acknowledgments

[47] We thank the captains, crew, and participants of the three cruises involved in collecting the seismic data: *R/V Atlantis* Voyage 7–36, *R/V Maurice Ewing* Cruise 03–09, and *R/V Knorr* Voyage 76 Leg IV. We are thankful to Jian Lin, B. E. Tucholke, Zhen Sun, and Andrew McCaig for helpful discussions. This research was supported by grants from the Chinese National Natural Science Foundation (41076029, 41176053, 91028002) and the U.S.-NSF (OCE-0137329). M.Z. was supported by China Scholarship Council for 6 months of cooperative research at WHOI. J.P.C. acknowledges support from The Andrew W. Mellon Foundation Endowed Fund for Innovative Research. The manuscript was improved by constructive reviews from Ingo Grevemeyer and an anonymous reviewer and by input from the Associate Editor.

References

Bach, W., and S. E. Humphris (1999), Relationship between the Sr and O isotope compositions of hydrothermal fluids and the spreading and magma-supply rates at oceanic spreading centers, *Geology*, *27*(12), 1067–1070, doi:10.1130/0091-7613(1999)027<1067:RBTSAO>2.3.CO;2.

Baines, A. G., M. J. Cheadle, B. E. John, and J. J. Schwartz (2008), The rate of oceanic detachment faulting at Atlantis Bank, SW Indian Ridge, *Earth Planet. Sci. Lett.*, *273*(1–2), 105–114, doi:10.1016/j.epsl.2008.06.013.

Blackman, D. K., et al. (2011), Drilling constraints on lithospheric accretion and evolution at Atlantis Massif, Mid-Atlantic Ridge 30°N, *J. Geophys. Res.*, *116*, B07103, doi:10.1029/2010JB007931.

Buck, W. R. (1988), Flexural rotation of normal faults, *Tectonics*, *7*, 959–973, doi:10.1029/TC007i005p00959.

Campbell, A. C., et al. (1988), Chemistry of hot springs on the Mid-Atlantic Ridge, *Nature*, *335*, 514–519, doi:10.1038/335514a0.

Canales, J. P. (2010), Small-scale structure of the Kane Oceanic Core Complex, Mid-Atlantic Ridge 23°30′N, from waveform tomography of multichannel seismic data, *Geophys. Res. Lett.*, *37*, L21305, doi:10.1029/2010GL044412.

Canales, J. P., R. A. Sohn, and B. deMartin (2007), Crustal structure of the Trans-Atlantic Geotraverse (TAG) segment (Mid-Atlantic Ridge, 26°10′N): Implications for the nature of hydrothermal circulation and detachment faulting at slow spreading ridges, *Geochem. Geophys. Geosyst.*, *8*, Q08004, doi:10.1029/2007GC001629.

Canales, J. P., B. E. Tucholke, M. Xu, J. A. Collins, and D. L. Dubois (2008), Seismic evidence for large-scale compositional heterogeneity of oceanic core complexes, *Geochem. Geophys. Geosyst.*, *9*, Q08002, doi:10.1029/2008GC002009.

Cannat, M. (1993), Emplacement of mantle rocks in the seafloor at mid-ocean ridges, *J. Geophys. Res.*, *98*, 4163–4172, doi:10.1029/92JB02221.

Cannat, M., et al. (1995), Thin crust, ultramafic exposures, and rugged faulting patterns at the Mid-Atlantic Ridge (22°-24°N), *Geology*, *23*, 49–52, doi:10.1130/0091-7613(1995)023<0049:TCUEAR>2.3.CO;2.

Carlson, R. L., and G. S. Raskin (1984), Density of the ocean crust, *Nature*, *311*, 555–558, doi:10.1038/311555a0.

Charlou, J.-L., and J.-P. Donval (1993), Hydrothermal methane venting between 12°N and 26°N along the Mid-Atlantic Ridge, *J. Geophys. Res.*, *98*(B6), 9625–9642, doi:10.1029/92JB02047.

Charlou, J. L., H. Bougault, P. Appriou, T. Nelsen, and P. Rona (1991), Different TDM/CH_4 hydrothermal plume signatures: TAG site at 26°N and serpentinized ultrabasic diapir at 15°05′N on the Mid-Atlantic Ridge, *Geochim. Cosmochim. Acta*, *55*, 3209–3222, doi:10.1016/0016-7037(91)90484-M.

Dannowski, A., I. Grevemeyer, C. R. Ranero, G. Ceuleneer, M. Maia, J. P. Morgan, and P. Gente (2010), Seismic structure of an oceanic core complex at the Mid-Atlantic Ridge, 22°19′N, *J. Geophys. Res.*, *115*, B07106, doi:10.1029/2009JB006943.

Dekov, V. (2006), Native nickel in the TAG hydrothermal field sediments (Mid-Atlantic Ridge, 26°N): Space trotter, guest from mantle, or a widespread mineral, connected with serpentinization, *J. Geophys. Res.*, *111*, B05103, doi:10.1029/2005JB003955.

deMartin, B. J., R. Reves-Sohn, J. P. Canales, and S. E. Humphris (2007), Kinematics and geometry of active detachment faulting beneath the Trans-Atlantic Geotraverse (TAG) hydrothermal field on the Mid-Atlantic Ridge, *Geology*, *35*(8), 711–714, doi:10.1130/G23718A.1.

Detrick, R. S., H. D. Needham, and V. Renard (1995), Gravity anomalies and crustal thickness variations along the Mid-Atlantic Ridge between 33°N and 40°N, *J. Geophys. Res.*, *100*, 3767–3787, doi:10.1029/94JB02649.

Dick, H. J. B., G. Thompson, and W. B. Bryan (1981), Low-angle faulting and steady-state emplacement of plutonic rocks at ridge-transform intersections, *Eos Trans. AGU*, *62*, 406.

Dick, H. J. B., M. A. Tivey, and B. E. Tucholke (2008), Plutonic foundation of a slow-spread ridge segment: Oceanic core complex at Kane Megamullion, 23°30′N, 45°20′W, *Geochem. Geophys. Geosyst.*, *9*, Q05014, doi:10.1029/2007GC001645.

Dunn, R. A., and D. R. Toomey (2001), Crack-induced seismic anisotropy in the oceanic crust across the East Pacific Rise (9°30′N), *Earth Planet. Sci. Lett.*, *189*, 9–17, doi:10.1016/S0012-821X(01)00353-3.

Dunn, R. A., V. Lekic, R. S. Detrick, and D. R. Toomey (2005), Three-dimensional seismic structure of the Mid-

Atlantic Ridge (35°N): Evidence for focused melt supply and lower crustal dike injection, *J. Geophys. Res.*, *110*, B09101, doi:10.1029/2004JB003473.

Edmonds, H. N., C. R. German, D. R. H. Green, Y. Huh, T. Gamo, and J. M. Edmond (1996), Continuation of the hydrothermal fluid chemistry time series at TAG, and the effects of ODP drilling, *Geophys. Res. Lett.*, *23*(23), 3487–3489, doi:10.1029/96GL01597.

Escartín, J., and J. P. Canales (2011), Detachments in oceanic lithosphere: Deformation, magmatism, fluid flow and ecosystems, *Eos Trans. AGU*, *92*(4), 31, doi:10.1029/2011EO040003.

Escartín, J., C. Mével, C. J. MacLeod, and A. M. McCaig (2003), Constraints on deformation conditions and the origin of oceanic detachments: The Mid-Atlantic Ridge core complex at 15°45′N, *Geochem. Geophys. Geosyst.*, *4*(8), 1067, doi:10.1029/2002GC000472.

Escartín, J., D. K. Smith, J. Cann, H. Schouten, C. H. Langmuir, and S. Escrig (2008), Central role of detachment faults in accretion of slow-spreading oceanic lithosphere, *Nature*, *455*, 790–794, doi:10.1038/nature07333.

Fujimoto, H., N. Seama, J. Lin, T. Matsumoto, T. Tanaka, and K. Fujioka (1996), Gravity anomalies of the Mid-Atlantic Ridge north of the Kane transform fault, *Geophys. Res. Lett.*, *23*, 3431–3434, doi:10.1029/96GL02080.

Garcés, M., and J. Gee (2007), Paleomagnetic evidence of large footwall rotations associated with low-angle faults at the Mid-Atlantic Ridge, *Geology*, *35*(3), 279–282, doi:10.1130/G23165A.1.

Henig, A. S., D. K. Blackman, A. J. Harding, J. P. Canales, and G. M. Kent (2012), Downward continued multi-channel seismic refraction analysis of Atlantis Massif oceanic core complex, 30°N Mid-Atlantic Ridge, *Geochem. Geophys. Geosyst.*, *13*, Q0AG07, doi:10.1029/2012GC004059.

Hooft, E. E. E., R. S. Detrick, D. R. Toomey, J. A. Collins, and J. Lin (2000), Crustal and upper mantle structure along three contrasting spreading segments of the Mid-Atlantic Ridge, 33.5°-35°N, *J. Geophys. Res.*, *105*, 8205–8226, doi:10.1029/1999JB900442.

Humphris, S. E., and J. R. Cann (2000), Constraints on the energy and chemical balances of the modern TAG and ancient Cyprus seafloor sulfide deposits, *J. Geophys. Res.*, *105*(B12), 28,477–28,488, doi:10.1029/2000JB900289.

Humphris, S. E., et al. (1995), The internal structure of an active sea-floor massive sulphide deposit, *Nature*, *377*, 713–716, doi:10.1038/377713a0.

Hussenoeder, S. A., G. M. Kent, and R. S. Detrick (2002), Upper crustal seismic structure of the slow spreading Mid-Atlantic Ridge, 35°N: Constraints on volcanic emplacement processes, *J. Geophys. Res.*, *107*(B8), 2156, doi:10.1029/2001JB001691.

Ildefonse, B., D. K. Blackman, B. E. John, Y. Ohara, D. J. Miller, C. J. MacLeod, and I. O. E. S. Party (2007), Oceanic core complexes and crustal accretion at slow-spreading ridges, *Geology*, *35*(7), 623–626, doi:10.1130/G23531A.1.

Karson, J. A., and H. J. B. Dick (1983), Tectonics of ridge-transform intersection at the Kane Fracture Zone, *Mar. Geophys. Res.*, *6*, 51–98, doi:10.1007/BF00300398.

Karson, J. A., and R. M. Lawrence (1997), Tectonic setting of serpentinite exposures on the western median valley wall of the MARK area in the vicinity of site 920, *Proc. Ocean Drill. Program Sci. Results*, *153*, 5–21.

Kleinrock, M. C., and S. E. Humphris (1996), Structural asymmetry of the TAG rift valley: Evidence from a near-bottom survey for episodic spreading, *Geophys. Res. Lett.*, *23*(23), 3439–3442, doi:10.1029/96GL03073.

Kong, L. S. L. (1990), Variations in structure and tectonics along the Mid-Atlantic Ridge, 23°N and 26°N, PhD thesis, 341 pp., Woods Hole Oceanogr. Inst., Mass. Inst. of Technol., Woods Hole.

Kong, L. S. L., S. C. Solomon, and G. M. Purdy (1992), Microearthquake characteristics of a mid-ocean ridge along-axis high, *J. Geophys. Res.*, *97*, 1659–1685, doi:10.1029/91JB02566.

Korenaga, J., W. S. Holbrook, G. M. Kent, P. B. Kelemen, R. S. Detrick, H.-C. Larsen, J. R. Hopper, and T. Dahl-Jensen (2000), Crustal structure of the southeast Greenland margin from joint refraction and reflection seismic tomography, *J. Geophys. Res.*, *105*, 21,591–21,614, doi:10.1029/2000JB900188.

Lalou, C., J.-L. Reyss, E. Brichet, M. Arnold, G. Thompson, Y. Fouquet, and P. A. Rona (1993), New age data from Mid-Atlantic ridge hydrothermal sites: TAG and Snakepit chronology revisited, *J. Geophys. Res.*, *98*, 9705–9713, doi:10.1029/92JB01898.

Lalou, C., J.-L. Reyss, E. Brichet, P. A. Rona, and G. Thompson (1995), Hydrothermal activity on a 10^5 year scale at a slow-spreading ridge, TAG hydrothermal field, Mid-Atlantic Ridge 26°N, *J. Geophys. Res.*, *100*, 17,855–17,862, doi:10.1029/95JB01858.

Langmuir, C., et al. (1997), Hydrothermal vents near a mantle hot spot: The Lucky Strike vent field at 37°N on the Mid-Atlantic Ridge, *Earth Planet. Sci. Lett.*, *148*, 69–91, doi:10.1016/S0012-821X(97)00027-7.

Lavier, L. L., W. R. Buck, and A. N. B. Poliakov (1999), Self-consistent rolling-hinge model for the evolution of large-offset low-angle normal faults, *Geology*, *27*(12), 1127–1130, doi:10.1130/0091-7613(1999)027<1127:SCRHMF>2.3.CO;2.

Lin, J., G. M. Purdy, H. Schouten, J.-C. Sempéré, and C. Zervas (1990), Evidence from gravity data for focused magmatic accretion along the Mid-Atlantic Ridge, *Nature*, *344*, 627–632, doi:10.1038/344627a0.

MacLeod, C. J., et al. (2002), Direct geological evidence for oceanic detachment faulting: The Mid-Atlantic Ridge, 15°45′N, *Geology*, *30*(10), 879–882, doi:10.1130/0091-7613(2002)030<0879:DGEFOD>2.0.CO;2.

MacLeod, C. J., R. C. Searle, B. J. Murton, J. F. Casey, C. Mallows, S. C. Unsworth, K. L. Achenbach, and M. Harris (2009), Life cycle of oceanic core complexes, *Earth Planet. Sci. Lett.*, *287*(3–4), 333–344, doi:10.1016/j.epsl.2009.08.016.

Magde, L. S., and D. W. Sparks (1997), Three-dimensional mantle upwelling, melt generation, and melt migration beneath segments of slow spreading ridges, *J. Geophys. Res.*, *102*(B9), 20,571–20,583, doi:10.1029/97JB01278.

Magde, L. S., A. H. Barclay, D. R. Toomey, R. S. Detrick, and J. A. Collins (2000), Crustal magma plumbing within a segment of the Mid-Atlantic Ridge, 35°N, *Earth Planet. Sci. Lett.*, *175*, 55–67, doi:10.1016/S0012-821X(99)00281-2.

McCaig, A. M., and M. Harris (2012), Hydrothermal circulation and the dike-gabbro transition in the detachment mode of slow seafloor spreading, *Geology*, *40*(4), 367–370, doi:10.1130/G32789.1.

McCaig, A. M., R. A. Cliff, J. Escartín, A. E. Fallick, and C. J. MacLeod (2007), Oceanic detachment faults focus very large volumes of black smoker fluids, *Geology*, *35*(10), 935–938, doi:10.1130/G23657A.1.

McCaig, A. M., A. Delacour, A. E. Fallick, T. Castelain, and G. Frueh-Green (2010), Detachment fault control on hydrothermal circulation systems: Interpreting the subsurface beneath the TAG hydrothermal field using the isotopic and geological evolution of oceanic core complexes in the

Atlantic, in *Diversity of Hydrothermal Systems on Slow Spreading Ocean Ridges*, *Geophys. Monogr. Ser.*, vol. 188, edited by P. A. Rona et al., pp. 207–239, AGU, Washington, D. C., doi:10.1029/2008GM000729.

Miller, D. J., and N. I. Christensen (1997), Seismic velocities of lower crustal and upper mantle rocks from the slow spreading Mid-Atlantic Ridge, south of the Kane transform zone (MARK), *Proc. Ocean Drill. Program Sci. Results*, *153*, 437–454.

Morris, A., J. S. Gee, N. Pressling, B. E. John, C. J. MacLeod, C. B. Grimes, and R. C. Searle (2009), Footwall rotation in an oceanic core complex quantified using reoriented integrated Ocean Drilling Program core samples, *Earth Planet. Sci. Lett.*, *287*(1–2), 217–228, doi:10.1016/j.epsl.2009.08.007.

Mutter, J. C., and J. A. Karson (1992), Structural processes at slow-spreading ridges, *Science*, *257*, 627–634, doi:10.1126/science.257.5070.627.

Nozaka, T., and P. Fryer (2011), Alteration of the oceanic lower crust at a slow-spreading axis: In sight from vein-related zoned halos in Olivine Gabbro from Atlantis Massif, Mid-Atlantic Ridge, *J. Petrol.*, *52*(4), 643–664, doi:10.1093/petrology/egq098.

Ohara, Y., K. Okino, and J. Kasahara (2007), Seismic study on oceanic core complexes in the Parece Vela back-arc basin, *Isl. Arc*, *16*, 348–360, doi:10.1111/j.1440-1738.2007.00591.x.

Okino, K., K. Matsuda, D. M. Christie, Y. Nogi, and K. Koizumi (2004), Development of oceanic detachment and asymmetric spreading at the Australian-Antarctic Discordance, *Geochem. Geophys. Geosyst.*, *5*, Q12012, doi:10.1029/2004GC000793.

Olive, J.-A., M. D. Behn, and B. E. Tucholke (2010), The structure of oceanic core complexes controlled by the depth distribution of magma emplacement, *Nat. Geosci.*, *3*(7), 491–495, doi:10.1038/ngeo888.

Palmer, M. R. (1996), Hydration and uplift of the oceanic crust on the Mid-Atlantic Ridge associated with hydrothermal activity: Evidence from boron isotopes, *Geophys. Res. Lett.*, *23*(23), 3479–3482, doi:10.1029/96GL02079.

Planert, L., E. R. Flueh, F. Tilmann, I. Grevemeyer, and T. Reston (2010), Crustal structure of a rifted oceanic core complex and its conjugate side at the MAR at 5°S: Implications for melt extraction during detachment faulting and core complex formation, *Geophys. J. Int.*, *181*(1), 113–126, doi:10.1111/j.1365-246X.2010.04504.x.

Pratt, R. G. (1999), Seismic waveform inversion in the frequency domain, Part 1: Theory and verification in a physical scale model, *Geophysics*, *64*(3), 888–901, doi:10.1190/1.1444597.

Reston, T. J., and C. R. Ranero (2011), The 3-D geometry of detachment faulting at mid-ocean ridges, *Geochem. Geophys. Geosyst.*, *12*, Q0AG05, doi:10.1029/2011GC003666.

Rona, P. A., G. Thompson, M. J. Mottl, J. A. Karson, W. J. Jenkins, D. Graham, K. L. Von Damm, and J. M. Edmond (1984), Hydrothermal activity at the Trans-Atlantic Geothermal Field, Mid-Atlantic ridge crest at 26°N, *J. Geophys. Res.*, *89*(B13), 11,365–11,377, doi:10.1029/JB089iB13p11365.

Rona, P. A., G. Klinkhammer, T. A. Nelsen, J. H. Trefry, and H. Elderfield (1986), Black smokers, massive sulphides and vent biota at the Mid-Atlantic Ridge, *Nature*, *321*, 33–37, doi:10.1038/321033a0.

Rona, P. A., Y. A. Bogdanov, E. G. Gurvich, N. A. Rimski-Korsakov, A. M. Sagalevitch, and M. D. Hannington (1993), Relict hydrothermal zones at the TAG hydrothermal field, Mid-Atlantic Ridge 26°N, 45°W, *J. Geophys. Res.*, *98*, 9715–9730, doi:10.1029/93JB00552.

Schouten, H., D. K. Smith, J. Cann, and J. Escartín (2010), Tectonic versus magmatic extension in the presence of core complexes at slow-spreading ridges from a visualization of faulted seafloor topography, *Geology*, *38*(7), 615–618, doi:10.1130/G30803.1.

Seher, T., W. C. Crawford, S. C. Singh, and M. Cannat (2010a), Seismic layer 2A variations in the Lucky Strike segment at the Mid-Atlantic Ridge from reflection measurements, *J. Geophys. Res.*, *115*, B07107, doi:10.1029/2009JB006783.

Seher, T., W. C. Crawford, S. C. Singh, M. Cannat, V. Combier, and D. Dusunur (2010b), Crustal velocity structure of the Lucky Strike segment of the Mid-Atlantic Ridge at 37°N from seismic refraction measurements, *J. Geophys. Res.*, *115*, B03103, doi:10.1029/2009JB006650.

Sempéré, J.-C., G. M. Purdy, and H. Schouten (1990), Segmentation of the Mid-Atlantic Ridge between 24°N and 30°40′N, *Nature*, *344*, 427–431, doi:10.1038/344427a0.

Smith, D. K., J. R. Cann, and J. Escartín (2006), Widespread active detachment faulting and core complex formation near 13°N on the Mid-Atlantic Ridge, *Nature*, *442*, 440–443, doi:10.1038/nature04950.

Smith, D. K., J. Escartín, H. Schouten, and J. R. Cann (2008), Fault rotation and core complex formation: Significant processes in seafloor formation at slow-spreading mid-ocean ridges (Mid-Atlantic Ridge, 13°-15°N), *Geochem. Geophys. Geosyst.*, *9*, Q03003, doi:10.1029/2007GC001699.

Sohn, R. A. (2007), Stochastic analysis of exit fluid temperature records from the active TAG hydrothermal mound (Mid-Atlantic Ridge, 26 N): 1. Modes of variability and implications for subsurface flow, *J. Geophys. Res.*, *112*, B07101, doi:10.1029/2006JB004435.

Sohn, R. A., S. C. Webb, J. A. Hildebrand, and B. D. Cornuelle (1997), Three-dimensional tomographic velocity structure of upper crust, CoAxial segment, Juan de Fuca Ridge: Implications for on-axis evolution and hydrothermal circulation, *J. Geophys. Res.*, *102*(B8), 17,679–17,695, doi:10.1029/97JB00592.

Tivey, M. A., H. Schouten, and M. C. Kleinrock (2003), A near-bottom magnetic survey of the Mid-Atlantic Ridge axis at 26°N: Implications for the tectonic evolution of the TAG segment, *J. Geophys. Res.*, *108*(B5), 2277, doi:10.1029/2002JB001967.

Tucholke, B. E., and J. Lin (1994), A geological model for the structure of ridge segments in slow spreading ocean crust, *J. Geophys. Res.*, *99*, 11,937–11,958, doi:10.1029/94JB00338.

Tucholke, B. E., J. Lin, and M. C. Kleinrock (1998), Megamullions and mullion structure defining oceanic metamorphic core complexes on the Mid-Atlantic Ridge, *J. Geophys. Res.*, *103*, 9857–9866, doi:10.1029/98JB00167.

Tucholke, B. E., M. D. Behn, R. Buck, and J. Lin (2008), The role of melt supply in oceanic detachment faulting and formation of megamullions, *Geology*, *36*(6), 455–458, doi:10.1130/G24639A.1.

Williams, C. M., M. A. Tivey, and M. D. Behn (2006), The magnetic structure of Kane megamullion: Results from marine magnetic anomalies, paleomagnetic data and thermal modeling, *Eos Trans. AGU*, *87*(52), Fall Meet. Suppl., Abstract T42A-03.

Xu, M., J. P. Canales, B. E. Tucholke, and D. L. Dubois (2009), Heterogeneous seismic velocity structure of the upper lithosphere at Kane oceanic core complex, Mid-Atlantic Ridge, *Geochem. Geophys. Geosyst.*, *10*, Q10001, doi:10.1029/2009GC002586.

Zelt, C. A., and P. J. Barton (1998), Three-dimensional seismic refraction tomography: A comparison of two methods applied to data from the Faeroe Basin, *J. Geophys. Res.*, *103*(B4), 7187–7210, doi:10.1029/97JB03536.

Zelt, C. A., and D. A. Forsyth (1994), Modeling wide-angle seismic data for crustal structure: Southeastern Grenville Province, *J. Geophys. Res.*, *99*, 11,687–11,704, doi:10.1029/93JB02764.

Zhang, J., U. S. ten Brink, and M. N. Toksöz (1998), Nonlinear refraction and reflection travel time tomography, *J. Geophys. Res.*, *103*, 29,743–29,757, doi:10.1029/98JB01981.

Zonenshain, L. P., M. I. Kuzmin, A. P. Lisitsin, Y. A. Bogdanov, and B. V. Baranov (1989), Tectonics of the Mid-Atlantic rift valley between the TAG and MARK areas (26°-24°N): Evidence for vertical tectonism, *Tectonophysics*, *159*, 1–23, doi:10.1016/0040-1951(89)90167-4.